Supporting Information

Functional Organic Binder Enhanced Vertical Graphene-Silicon Based Anodes for High-Performance Lithium-Ion Batteries

Hongyan Wang,* Zixin Zhu, Yongxing Su, Guizhi Wang, Xingpeng Du, Fan Xie and Xiang Li

Key Laboratory of Spin Electron and Nanomaterials of Anhui Higher Education Institutes, School of Chemistry and Chemical Engineering, Suzhou University, Suzhou, Anhui 234000, P. R. China.

*Email addresses of corresponding authors: szxybattery@163.com

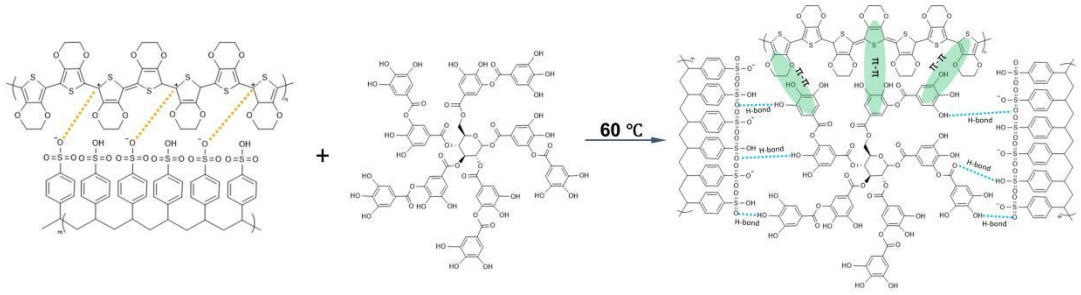

Figure S1. The mechanism diagram of the chemical reaction process for TA and PEDOT:PSS, which illustrates the hydrogen bonding and π-π conjugation interactions in detail.

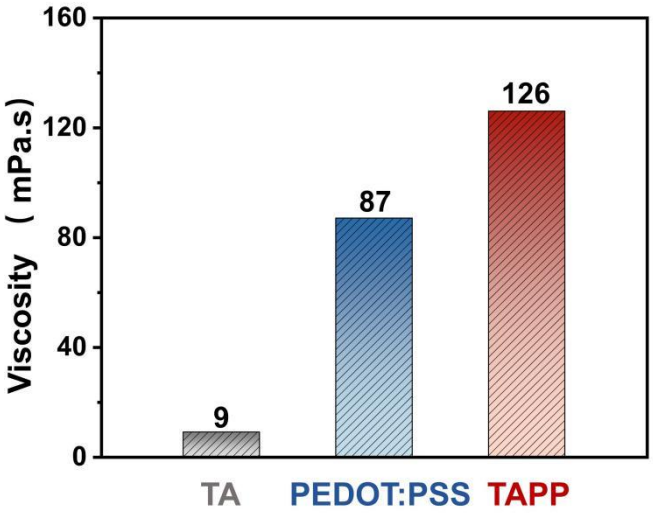

Figure S2. The viscosity of the TA solution, the PEDOT:PSS solution and the TAPP solutions. The results show that the addition of TA leads to a increase in solution viscosity. This observation provides direct rheological evidence for the formation of a supramolecular cross-linked network between TA and PEDOT:PSS.

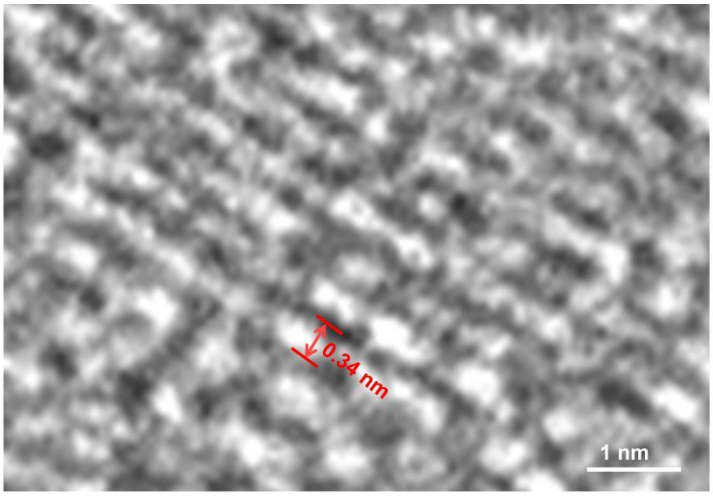

Figure S3. High-resolution transmission electron microscopy (HRTEM) of the VG in the SiVG/TAPP anode reveals lattice fringes with a spacing of approximately 0.34 nm, which is characteristic of the (002) plane of graphene.

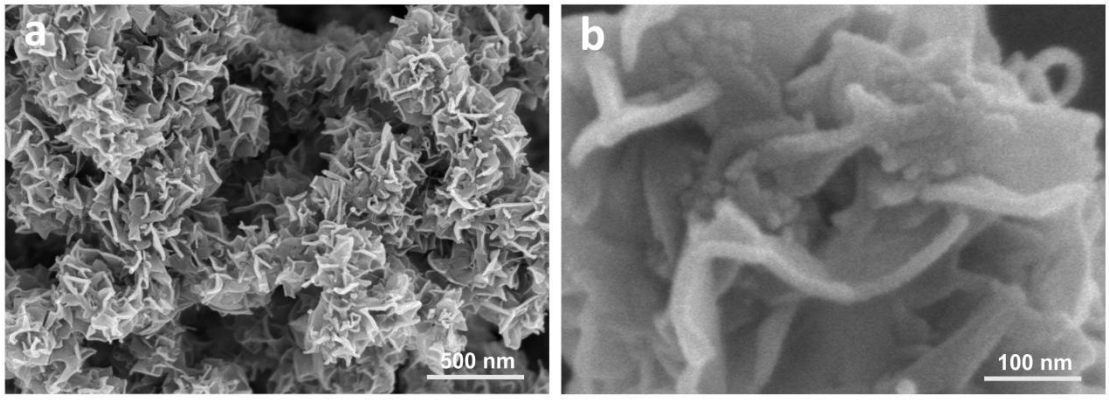

Figure S4. The scanning electron microscope (SEM) of the SiVG confirms the successful in situ growth of wrinkled VG on Si surfaces.

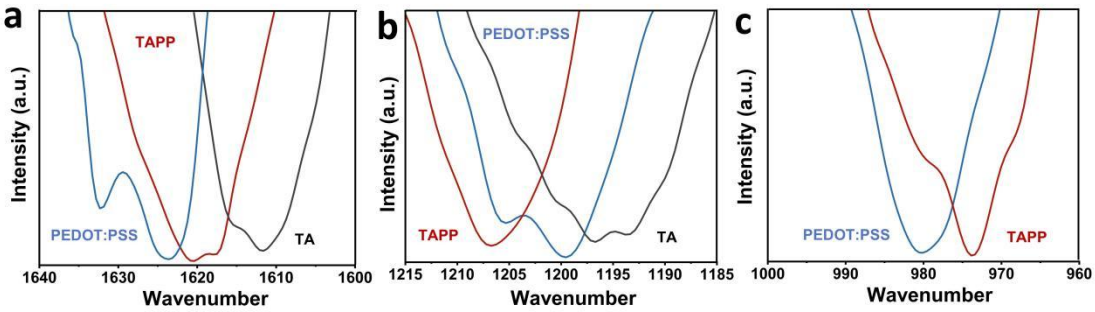

Figure S5. Fourier transform infrared spectroscopy (FTIR) spectra of TA, PEDOT:PSS and the TAPP composite. The TAPP composite shows shifts in -C=O (1620 cm^{-1}), and sulfonic acid (-SO_3H) vibrations (1207 cm^{-1}), indicating strong hydrogen bonding between TA and PEDOT:PSS. The thiophene C-S stretch shifts to 971 cm^{-1}, likely due to π-π conjugation with the benzene ring.

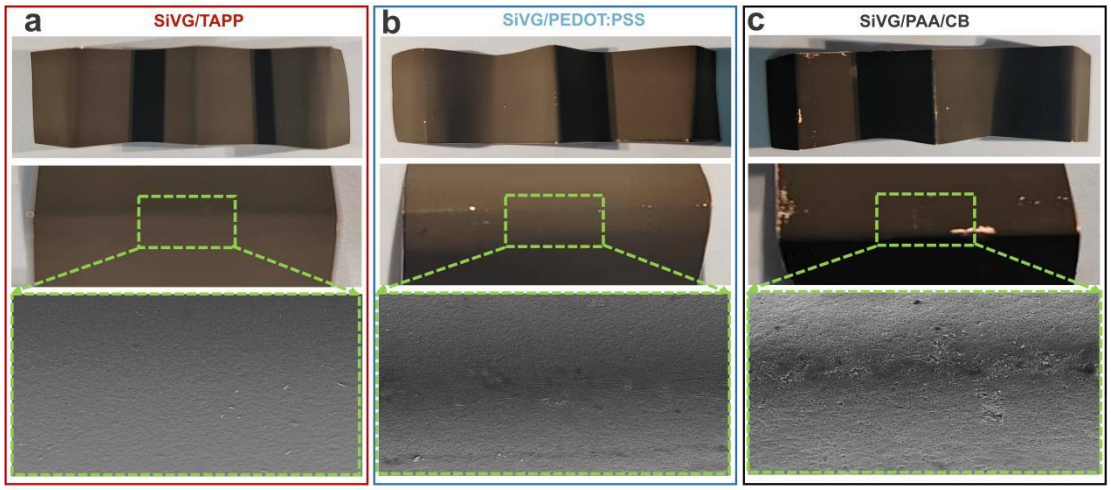

Figure S6. The photographs and SEM images of the bending experiment show that SiVG/TAPP anode maintains its morphology, while SiVG/PEDOT:PSS and especially SiVG/PAA/CB anodes suffer damage. The results confirm that cross-linking TA with PEDOT:PSS enhances the mechanical strength of SiVG-based anodes for high-performance applications.

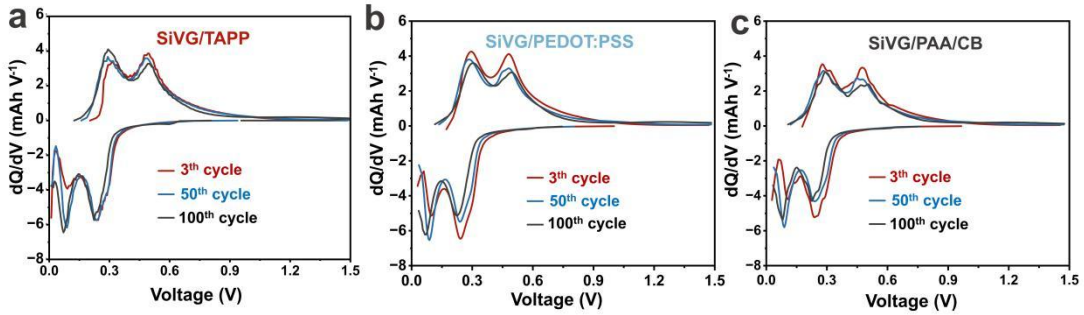

Figure S7. The differential capacity (dQ/dV) curves for the 3th, 50th and 100th cycle of (a) SiVG/TAPP, (b) SiVG/PEDOT:PSS and (c) SiVG/PAA/CB anodes. In discharge, the 0.03-0.3 V peak is from SiVG-lithium alloying, with the 0.23 V peak reflecting $Li_{14}Si_6$ and $Li_{13}Si_4$. At 0.07 V, the products transition to $Li_{13}Si_4$/$Li_{15}Si_4$. Charging shows peaks in the 0.3-0.5 V range, indicating the delithiation and dealloying of Li–Si alloys to amorphous silicon.

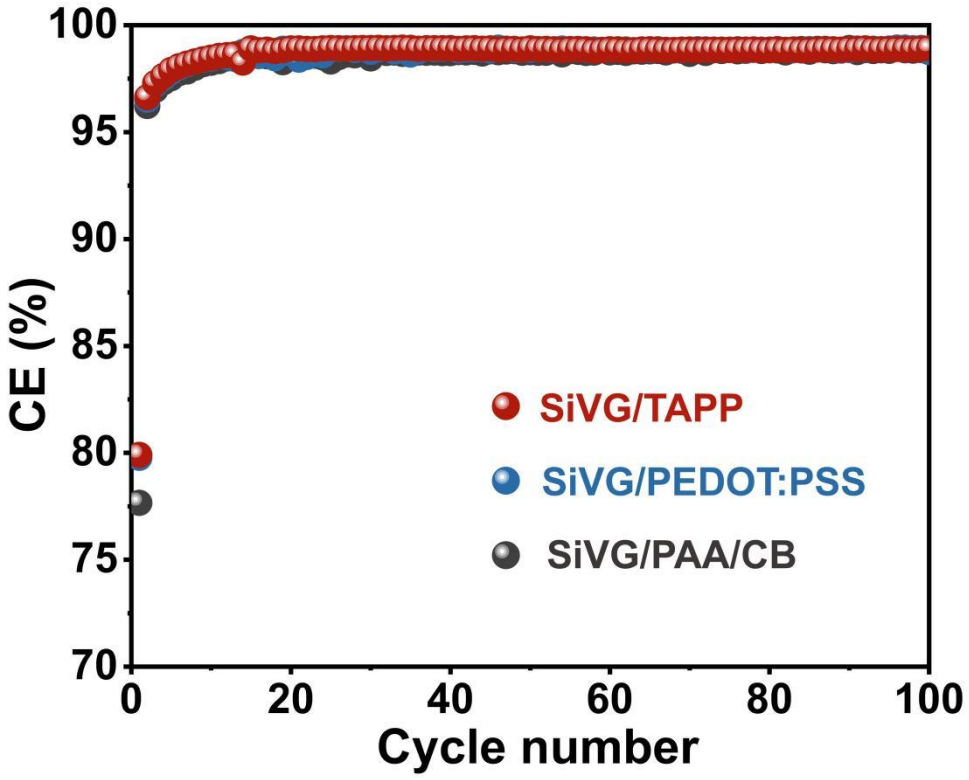

Figure S8. The CE of the SiVG/TAPP, SiVG/PEDOT:PSS and SiVG/PAA/CB anodes.The SiVG/TAPP anode achieves a Coulombic efficiency of 79.90%, surpassing SiVG/PEDOT:PSS (79.76%) and SiVG/PAA/CB (77.66%).

Table S1. A comparison of the electrochemical performance between the SiVG/TAPP anode and recently published Si-based anodes.

Binder	**Binder ratio (wt%)**	**Loading (mg cm^{-2})**	**Cycling performance (Retention rate& Remaining capacity)**	**Ref.**
SiVG/TAPP	85/15	~0.7	86.9% 2449.3 mAh g^{-1} (1 A g^{-1}, 100 cycles)	**This work**
H-Si/LPAA/AC	70/15/15	0.8-1.0	83.7% & 2107.6 mAh g^{-1} (1 A g^{-1}, 100 cycles)	**Ref.**1
Si@PEI/PR(D2000)/SP	60/20/20	~1.0	50.7% & 2025.1 mAh g^{-1} (0.2 C & 0.84 A g^{-1}, 100 cycles)	**Ref.2**
Si@PVA@LB20	80/10/10	0.7–0.9	2095 mAh g^{-1} (1 A g^{-1}, 100 cycles)	**Ref.3**
Si/HM/SP	60/10/30	0.5	59.9% & 1949 mAh g^{-1} (0.1C & 0.42 A g^{-1}, 100 cycles)	**Ref.4**

μSi/SWCNTs/ TUEG-OH-PAA	80/10/10	0.6–0.8	75.5% & 2447 mAh g^{-1} (1.2 A g^{-1}, 100 cycles)	**Ref.5**
Si/PVA-MA/SP	60/20/20	~1.5	62% & 2267 mAh g^{-1} (0.3 C& 1.26 A g^{-1}， 100 cycles）	**Ref.6**
Si/c-POAH/SP	80/10/10	~0.65	67.1% & 2184.7 mAh g^{-1} (0.84 A g^{-1}, 100 cycles)	**Ref.7**

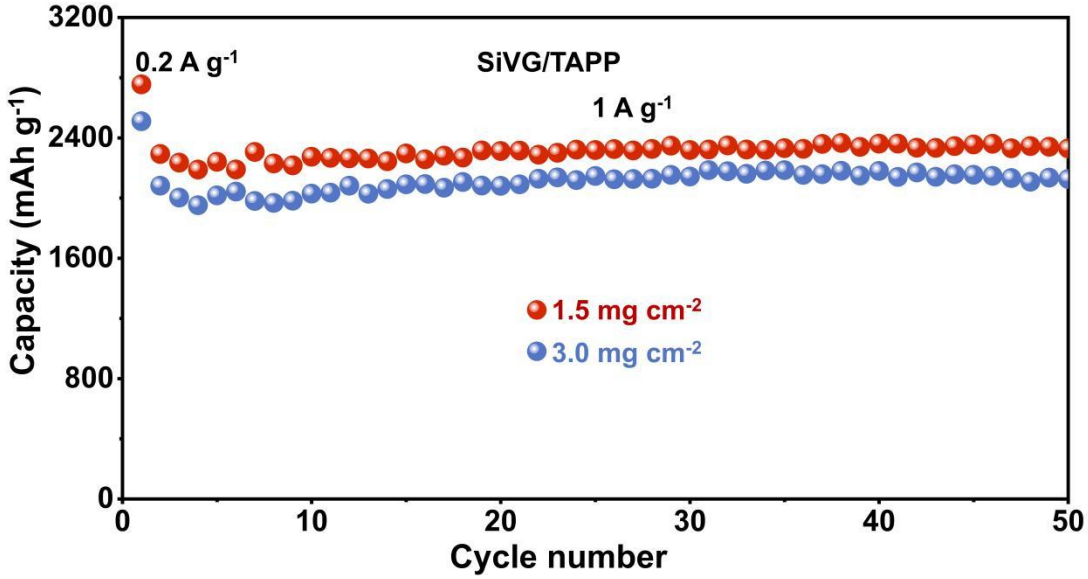

Figure S9. The cyclic performance of the SiVG/TAPP anode at loadings of 1.5 mg cm^{-2} and 3.0 mg cm^{-2}. The SiVG/TAPP anode retains excellent electrochemical performance over 50 cycles at loadings of 1.5 mg cm^{-2} and 3.0 mg cm^{-2}, with capacity retention rates of 88.6% and 87.2%, respectively, demonstrating its practical and commercial potential.

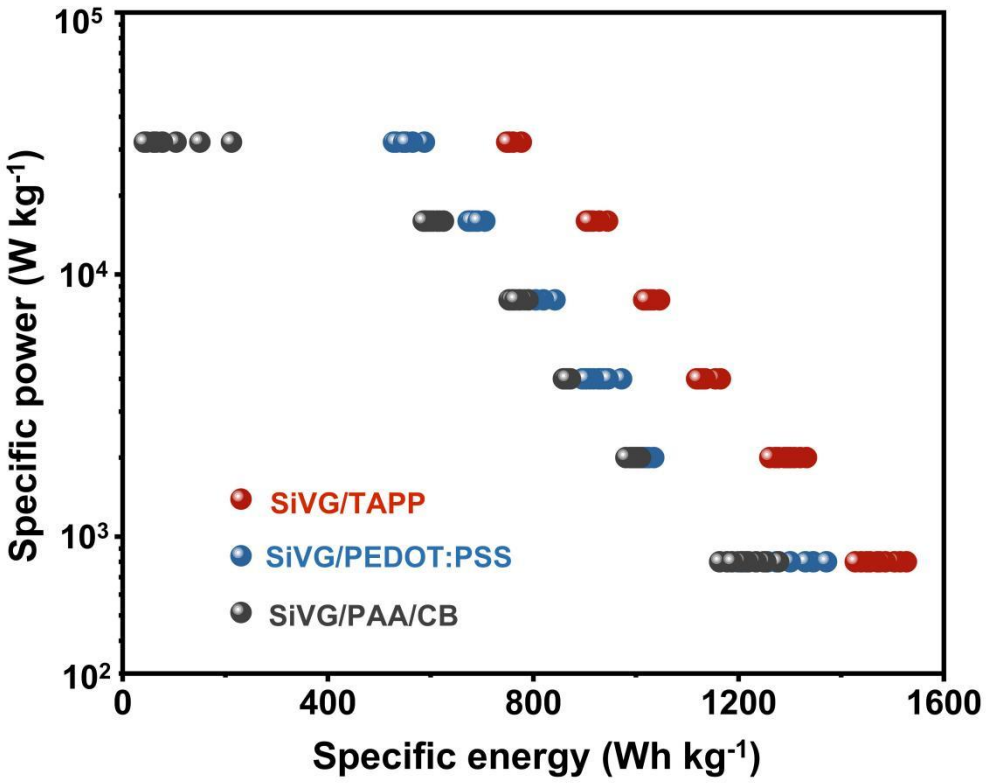

Figure S10. The Ragone plots (energy density vs. power density) of the SiVG/TAPP, SiVG/PEDOT:PSS and SiVG/PAA/CB anodes. The Ragone plot reveals that the SiVG/TAPP anode achieves 750 Wh kg^{-1} at 3.2×10^4 W kg^{-1}, demonstrating its suitability for fast-charging batteries.

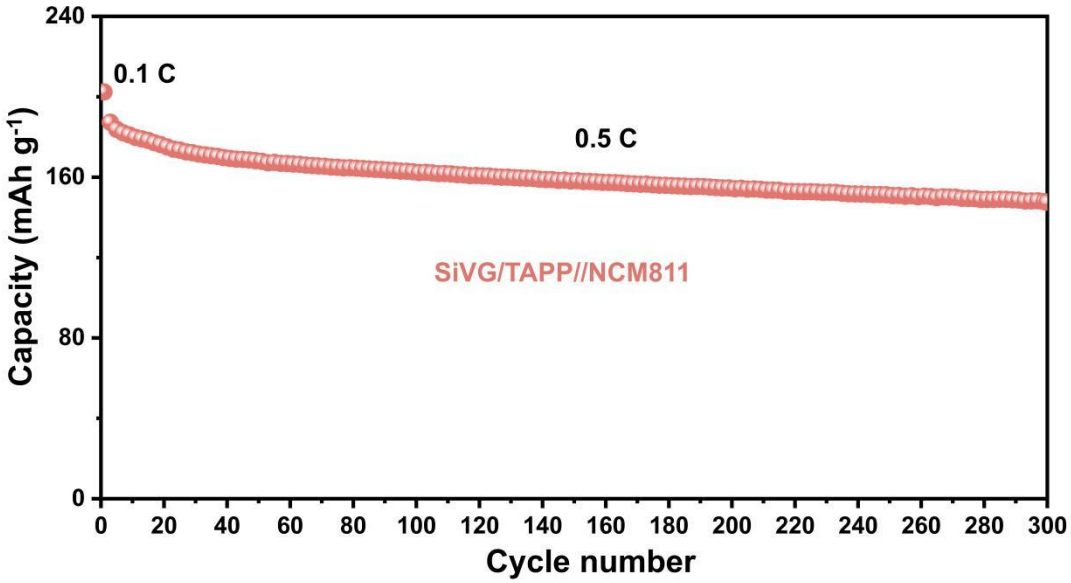

Figure S11. The the cyclic performance of full cell (SiVG/TAPP//NCM811). After 300 cycles, the full cell maintains 147.5 mAh g^{-1} (78.0% of initial capacity), with a decay rate of 0.073% per cycle, highlighting the electrode design's durability.

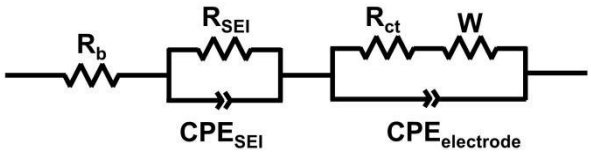

Figure S12. Equivalent circuit model of lithium-ion half-cell. In the equivalent circuit, Rb denotes the resistance of bulk materials (current collector, electrolyte, separator), reflected in Zreal on the Nyquist plot. W impedance, linked to lithium-ion diffusion in the anode, is derived from the slope after the arc. R_{SEI} arises from the layer impedance formed between the electrode and electrolyte from electrolyte decomposition. R_{ct} reflects the electrochemical reaction kinetics, influenced by particle size, surface coating, band gap, and phase transition.

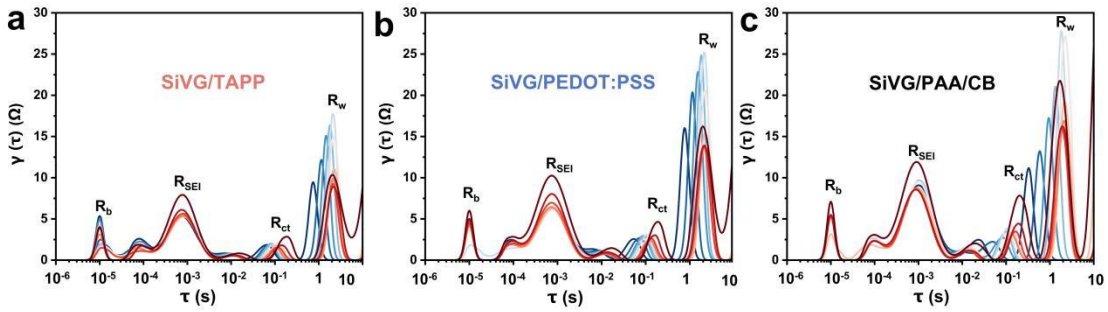

Figure S13. In situ distribution of relaxation times (DRT) curves of SiVG/TAPP, SiVG/PEDOT:PSS and SiVG/PAA/CB anodes. The peaks of the DRT curves correspond to specific reaction steps. The SiVG/TAPP exhibits the lowest peak intensities in the intervals of 10^{-4}-10^{-3} s (R_{SEI}) and 10^{-2}-1 s (R_{ct}), whereas SiVG/PAA/CB demonstrates the highest intensities.

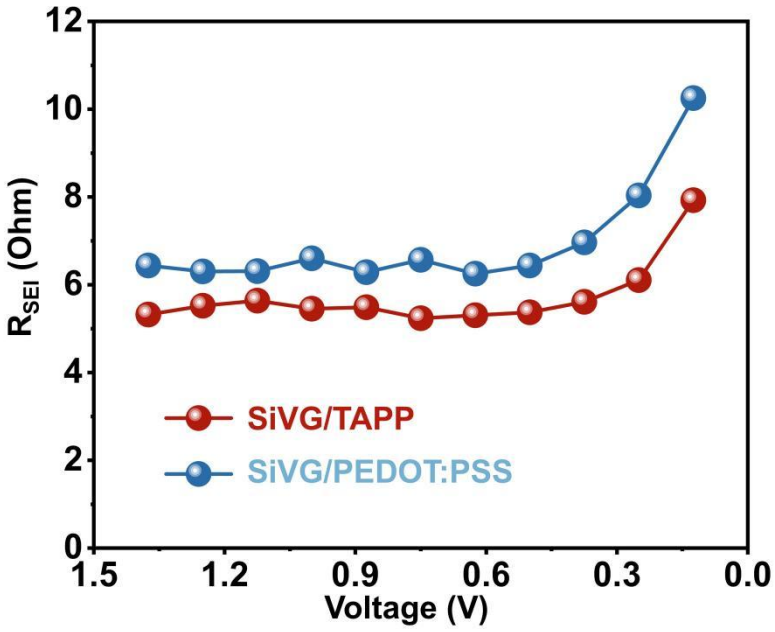

Figure S14. The R_{SEI} of SiVG/TAPP and SiVG/PEDOT:PSS anodes during lithiation processes. The fitted data reveals that the SiVG/TAPP electrode has a lower average R_{SEI} (5.7 Ohm) compared to SiVG/PEDOT:PSS (6.9 Ohm), indicating enhanced ionic conductivity of the SEI layer with the TA-modified binder.

References

1 S.-H. Guo, T. Li and Y.-J. Bai, *J. Energy Storage*, 2024, **101**, 113804.

2 X. W. Liu, J. X. Zhu, X. Y. Zeng, H. R. Zhu, Z. Deng, L. Ma, J. L. Lan, Y. H. Yu and

X. P. Yang, *J. Power Sources*, 2025, **658**, 238196.

3 X. X. Wang, K. Wang, Z.W. Wan, Y. H. Weng, Z.F. Zheng, J. Zhao, H. Li, D. Qian, Z.Y. Wu, M. Ling and C. D. Liang, *Mater. Today Energy*, 2024, **43**, 101567.

4 W. Ai, C. Yang, Q. Wang, W. Han, Y. Wang, J. Hou, Z. Zhu, J. Zhao, Y. Zhang, Y. Zhang and X. Li, *Langmuir*, 2025, **41**, 9469–9479.

5 H. Li, X. Li, K. Zhang, D. Liu, Y. Wang, G. Zhu, C. Hu, B. Zhang and W. Zhou, *Adv. Funct. Mater.*, 2025, 2505500.

6 T. H. Lee, B. S. Reddy, H. J. Na, J. H. Kim, G. B. Cho, J. H. Ahn, H. J. Ahn and K. K. Cho, *ACS Appl. Energy Mater.*, 2025, **8**, 332–342.

7 J. Xue, S. Jia, T. Xiang, J. Zhou and L. Li, *ACS Appl. Mater. Interfaces*, 2024, **16**, 38458–38465.